TOC:

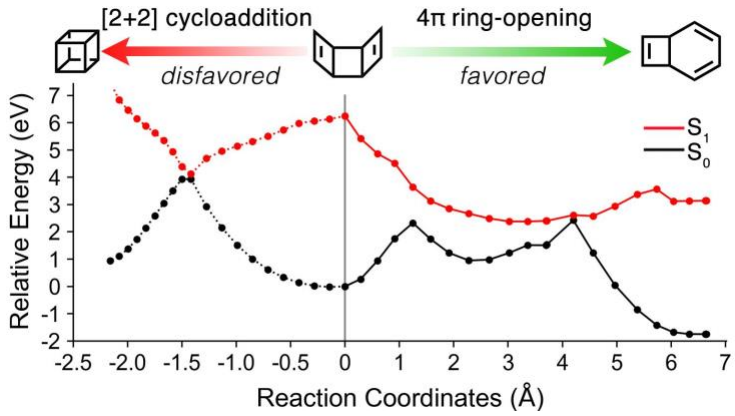

Multiconfigurational Static and Dynamic Calculations Explain Tricyclo[4,2,0,0$_{2,5}$]octa-3,7-diene Photochemistry

Jingbai Li and Steven A. Lopez*

Department of Chemistry & Chemical Biology, Northeastern University, 360 Huntington Ave, Boston MA, 02115

*steven.lopez@northeastern.edu

Abstract:

Sunlight is a renewable energy source that can be stored in chemical bonds using photochemical reactions. The synthesis of exotic and strained molecules is especially attractive with photochemical techniques because of the associated efficient and mild reaction conditions. We have used complete active space self-consistent field (CASSCF) calculations with an (8,7) active space and the ANO-S-VDZP basis set to understand the photophysics and subsequent photochemistry of a possible cubane precursor tricyclo[4,2,0,0$_{2,5}$]octa-3,7-diene (**1**). The energies were corrected with a second-order perturbative correction CASPT2(8,7)/ANO-S-VDZP. The $S_0 \rightarrow S_1$ vertical excitation energy of **1** is 6.25 eV, whose nature is $\pi \rightarrow \pi^*$ excitation. The minimum energy path from the S_1 Franck-Condon point leads directly to a 4π-disrotatory electrocyclic ring-opening reaction to afford bicyclo[4,2,0]octa-2,4,7-triene. The 2D potential energy surface scan located a rhomboidal S_1/S_0 minimum energy crossing point that connects **1** and cubane, suggesting that a cycloaddition is theoretically possible. We used the fewest switches surface hopping to study this reaction: 85% of 1,722 trajectories relaxed to 8 products; the major products are bicyclo[4,2,0]octa-2,4,7-triene (30%) and cycloocta-1,3,5,7-tetraene (32%). Only 0.4% of trajectories undergo a [2+2] cycloaddition to form cubane.

Introduction

Organic photochemical reactions are attractive because they typically require mild conditions and or low-cost reagents while offering high chemo- and stereoselectivities. They are routinely used to build strained, exotic molecular architectures with applications in natural product synthesis,[1] materials chemistry,[2] and photopharmacology.[3] Materials chemists have harnessed solar energy for solar fuels and solar thermal storage.[4] These processes convert light into chemical energy that can be made in possible portable energy storage materials. One promising example is cubane; it is O_h symmetric and has physical properties incongruous with other hydrocarbons. Cubane is highly strained (161.5 kcal·mol^{-1})[5] because of the eight methine (CH) units arranged in a cube; this also leads to a relatively high density (ρ = 1.29 g·cm^{-3}),[6] whereas the density of *n*-pentane is 0.63 g·cm^{-3}.[7] Interestingly, cubane is thermally stable at room temperature[8] and under high pressures,[9] making it an excellent candidate as a propellant. Recent programmable arylation of cubane has accessed a new arylcubane family that further extended the application as functional materials and pharmaceuticals.[10]

Substituted tricyclo[4,2,0,0^{2,5}]octa-3,7-dienes (TODs) have been used in [2+2] cycloadditions to afford substituted cubanes. This one-step routine with light-irradiation at 20–80 °C would be more straightforward than Eaton and Cole's original synthetic protocol.[11] Scheme 1 shows examples of photochemically synthesized cubanes, including octamethylcubane,[12] propellacubane,[13] and octa(trifluoromethyl)cubane.[14] Meijere and co-workers have reported the conversion of octacyclopropylcubane from the TOD precursor under mild conditions (20 °C, 3hrs) with a relatively high yield of 48%.[15]

Scheme 1. The photochemical synthesis of substituted cubanes from TOD precursors.

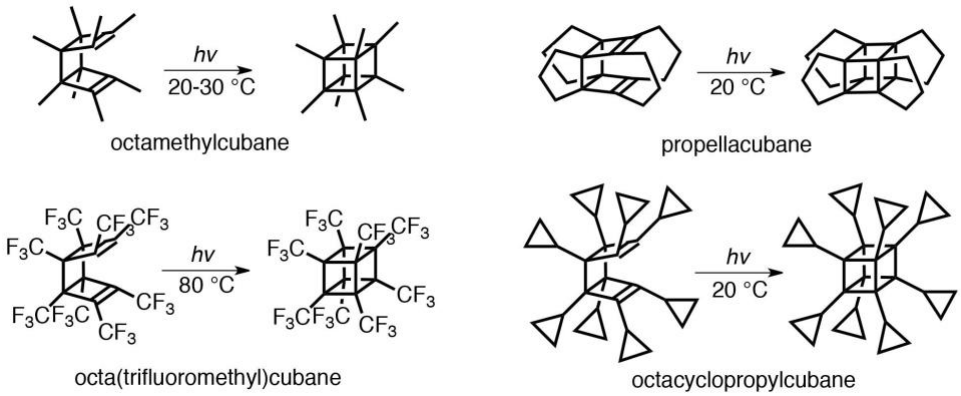

The [2+2] photocycloaddition of unsubstituted tricyclo[4,2,0,0^{2,5}]octa-3,7-dienes (**1**) has not been experimentally reported. Gleiter and co-workers find the [2+2] photocycloaddition via the lowest-energy photo-excitation of **1** is symmetry forbidden[16] using then-contemporary methods such as AM1[17] and Hartree-Fock with the 3-21G basis set. Through-space orbital interactions between the π- and σ-orbitals of the tricyclic framework were shown to rearrange the frontier molecular orbitals (FMOs) as shown in Scheme 2.[16] Gleiter explains that the lowest-energy transition in the TOD

precursor of propellacubane (Scheme 1) is symmetry-allowed because the reduced through-bond interactions lead to rearranged FMOs and an observed [2+2] photocycloaddition.[16, 18]

Scheme 2. Frontier molecular orbitals diagram of **1**.

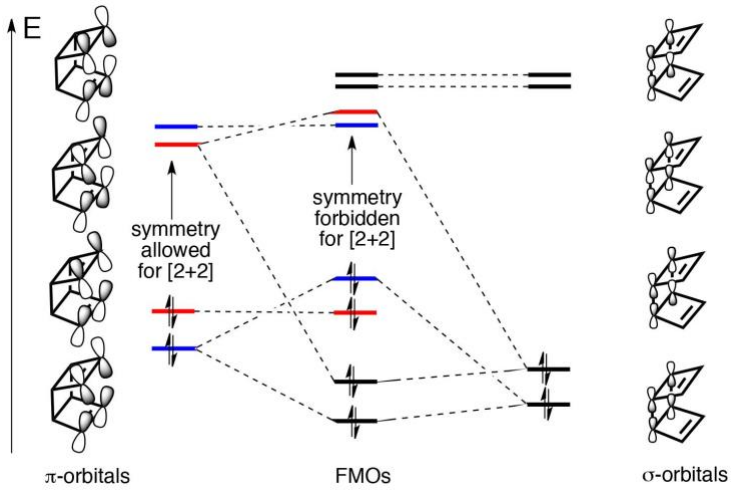

We have now used multiconfigurational complete active space self-consistent field (CASSCF) with single- and extend-multistate second-order perturbative corrections (CASPT2 and XMS-CASPT2, respectively) calculations to understand the photophysics and subsequent photochemistry of **1**. We demonstrate the importance of active space selection in CASSCF calculations to enumerate the possible photochemical pathways of **1**. We performed minimum energy path calculations and 2D potential energy surface (PES) scans to determine the possible photochemical outcomes of irradiating **1**. Subsequent simulations with fewest switches surface hopping (FSSH) non-adiabatic molecular dynamics (NAMD) were performed on **1** for the first time to comprehensively enumerate reaction pathways and identify dynamic effects.

Computational Details

Multiconfigurational methods

The multiconfigurational calculations were performed with state-averaged complete active space self-consistent field (SA-CASSCF) using OpenMolcas.19.11.[19] We used SA(*N*)-CASSCF(*m*,*n*) to describe the used methods, where *N* denotes the number of equally weighted singlet states, *m* and *n* are the number of electrons and orbitals in the active space, respectively. We compared two active spaces, (4,4) and (8,7). Our (4,4) active space features 4 π-electrons, 2 π-, and π*-orbitals (Figure 1a). The CASSCF(8,7) has two additional pairs of σ- and σ*-orbitals but omits the highest-lying antibonding π*-orbital (Figure 1b).

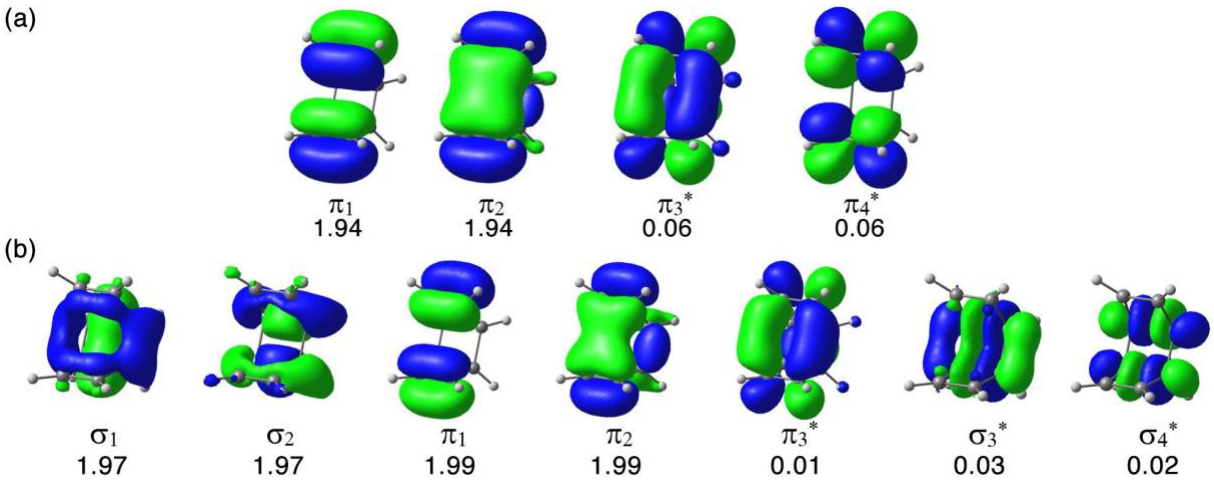

Figure 1. (a) CASSCF(4,4) active space and (b) CASSCF(8,7) active space of **1**. The orbitals are computed at SA(2)-CASSCF(4,4)/ANO-S-VDZP and SA(5)-CASSCF(8,7)/ANO-S-VDZP level of theory, respectively. Isosurface value = 0.04.

The ground-state geometry of **1** (**1-S$_0$**) was optimized with both active spaces and the ANO-S-VDZP basis set.[20] Vibrational analysis of all stationary points confirmed them as (no negative frequencies for minima). The electronic energies were corrected with complete active space second-order perturbation theory (CASPT2) and extended-multistate CASPT2 (XMS-CASPT2) with the corresponding active spaces and basis set. These calculations included a shift of (0.200 Hartrees or 5.4 eV) to avoid intruder states.[21]

Excitation energies

We compared our CASSCF/ANO-S-VDZP, CASPT2/ANO-S-VDZP//CASSCF/ANO-S-VDZP, and XMS-CASPT2/ANO-S-VDZP//CASSCF/ANO-S-VDZP vertical excitation energies with the cited active spaces to those computed by a variety of single reference time-dependent density functional theory (TD-DFT) calculations including using range-separated density functionals (CAM-B3LYP[22] and ωB97X[23]), equation-of-motion coupled-cluster singles doubles (EOM-CCSD),[24] and domain-based local pair natural orbital similarity transformed equation of motion-coupled cluster singles and doubles (DLPNO-STEOM-CCSD)[25] with the cc-pVDZ basis set[26] based on PBE0[27]/cc-pVDZ optimized geometries. The DFT, TD-DFT, and DLPNO-STEOM-CCSD calculations were carried out by ORCA. 4.2.1.[28] The EOM-CCSD calculation used Gaussian 16.[29]

Potential energy surface and reaction coordinate diagram

The minimum energy path (MEP) calculations were performed starting from the S$_1$ Franck-Condon point of **1** (**1-S$_1$-FC**) using SA(5)-CASSCF(8,7)/ANO-S-VDZP. The MEP calculation led directly to an S$_1$/S$_0$ minimum energy crossing point, **1-MECP-1**. The geometry of **1-MECP-1** was optimized at SA(4)-CASSCF(8,7)/ANO-S-VDZP to circumvent unstable geometry optimizations with 5 state-averaged wavefunctions. Single point energy calculations were performed on this

geometry with SA(5)-CASSCF(8,7)/ANO-S-VDZP. The following MEP calculation started from the ground-state at **1-MECP-1** and relaxed to bicyclo[4,2,0]octa-2,4,7-triene (**3**), which was confirmed with a SA(5)-CASSCF(8,7)/ANO-S-VDZP geometry optimization.

The 2D PES scans were computed along S_1 to understand the topology of the excited-state surface. The scans coordinates constrained the two reaction coordinates of **1-S$_1$-FC** (Figure 2): 1) *r*, which represents the distance between C1 and C3 (C2 and C4) and ranges from 1.8–2.5 Å with a step size of 0.05 Å and 2) θ, which represents the angle formed by C3-C1-C2 (C2-C4-C3) and ranges from 64 to 85° with a step size of 1.5 °. The PES served as a map to locate the S_1/S_0-MECP relevant to possible cycloaddition path.

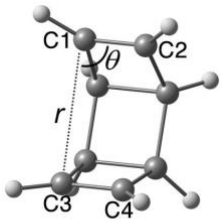

1-S$_1$-FC

Figure 2. The two reaction coordinates in **1-S$_1$-FC** used for the 2D PES scan. Note **1-S$_1$-FC** shares the same geometry and active space of **1-S$_0$** optimized at SA(5)-CASSCF(8,7)/ANO-S-VDZP level of theory.

The scan switches to an MECP optimization if it fails to optimize a point in the S_1 surface near an S_1/S_0 degeneracy (defined as an S_0–S_1 energy difference of <0.8 eV). Then the MECP is relaxed without geometrical constraints, named as **1-MECP-2**. The branching planes of the **1-MECP-1** and **1-MECP-2** are characterized by two orthogonal vectors: the difference of energy gradient vector (*g*-vector) and the non-adiabatic coupling vector (*h*-vector). The PESs near **1-MECP-1** and **1-MECP-2** were scanned over the branching plane at the same level as their MECP optimizations, respectively, along with the radii (0–0.05 Å) at 0.01 Å per step and around the center at 10° per step. The reaction coordinate diagram was computed to demonstrate the hypothetical reaction path towards cubane (**2**). 20 geometries in the diagram were interpolated by varying the redundant internal coordinates of **1-S$_1$-FC** to that of **1-MECP-2** and to that of **2** in equal-spaced increments

Fewest switches surface hopping non-adiabatic molecular dynamics

The fewest switches surface hopping non-adiabatic molecular dynamics (FSSH-NAMD) simulations were performed at the SA(5)-CASSCF(8,7)/ANO-S-VDZP level of theory as implemented in OpenMolcas 19.11.[19] Wigner sampling was used to generate the initial conditions of **1** in the S_1 Franck-Condon region. 1722 trajectories were propagated at 300 K (Nosé-Hoover thermostat[30]) for 2800 a.u. with a 20 a.u. time step (~700 and 0.5 fs, respectively).

Results and Discussion

We benchmarked the vertical excitation energies of **1** with single-reference and multiconfigurational methods, including an exploration of two active spaces for the CASSCF calculations. This is an important step in performing CASSCF calculations, which are not "black-box" and depend on active space choice. We compared these energies to those computed with range-separated density functionals CAM-B3LYP and ωB97XD. These have been shown to correctly predict the excitation energies of organic molecules.[31] We also included EOM-CCSD and DLPNO-STEOM-CCSD methods in our benchmarking because of their inclusion of doubly-excited configurations. We computed vertical excitation energies with the (4,4) and (8,7) active spaces. Vertical excitation energies are usually overestimated with CASSCF because the method neglects dynamic electron energy. However, second-order perturbative corrections such as CASPT2 and XMS-CASPT2 corrections account for dynamic correlation and result in predictive excitation energies. These results are summarized in Table 1.

Table 1. The vertical excitation energies, oscillator strength and electronic transitions of **1** at different levels of theory.*a*

Method	Energy (eV)			Oscillator strength			Transition		
	S_1	S_2	S_3	S_1	S_2	S_3	$S_0 \rightarrow S_1$	$S_0 \rightarrow S_2$	$S_0 \rightarrow S_3$
CAM-B3LYP	6.36	6.48	6.99	0.04	0.00	0.00	$\pi_2 \rightarrow \pi_3^*$	$\sigma_2 \rightarrow \pi_3^*$	$\sigma_2 \rightarrow \pi_4^*$
ωB97XD	6.50	6.57	7.15	0.04	0.00	0.00	$\pi_2 \rightarrow \pi_3^*$	$\sigma_2 \rightarrow \pi_3^*$	$\pi_2 \rightarrow \pi_4^*$
DLPNO-STEOM-CCSD	6.69	6.77	7.19	0.08	0.00	0.00	$\pi_2 \rightarrow \pi_3^*$	$\sigma_2 \rightarrow \pi_3^*$	$\pi_2 \rightarrow \pi_4^*$
EOM-CCSD	6.90	7.02	7.42	0.04	0.00	0.00	$\pi_2 \rightarrow \pi_3^*$	$\sigma_2 \rightarrow \pi_3^*$	$\pi_2 \rightarrow \pi_4^*$
SA(6)-CASSCF(4,4)	8.43	8.57	8.77	0.00	0.00	0.48	$\pi_1 \rightarrow \pi_3^*$	π_1, $\pi_2 \rightarrow \pi_3^*$, π_4^*	$\pi_2 \rightarrow \pi_3^*$
CASPT2(4,4)	6.50	6.75	6.95				$\pi_2 \rightarrow \pi_3^*$	$\pi_1 \rightarrow \pi_3^*$	$\pi_2 \rightarrow \pi_4^*$
XMS-CASPT2(4,4)	6.51	6.77	7.22				$\pi_2 \rightarrow \pi_3^*$	$\pi_1 \rightarrow \pi_3^*$	$\pi_2 \rightarrow \pi_4^*$
SA(5)-CASSCF(8,7)	7.74	7.87	8.32	0.24	0.00	0.00	$\pi_2 \rightarrow \pi_3^*$	$\pi_1 \rightarrow \pi_3^*$	$\sigma_2 \rightarrow \pi_3^*$
CASPT2(8,7)	6.25	6.39	6.75				$\pi_2 \rightarrow \pi_3^*$	$\sigma_2 \rightarrow \pi_3^*$	$\pi_1 \rightarrow \pi_3^*$
XMS-CASPT2(8,7)	6.03	6.53	7.08				$\sigma_2 \rightarrow \pi_3^*$	$\pi_2 \rightarrow \pi_3^*$	$\pi_1 \rightarrow \pi_3^*$

[a]The CAM-B3LYP, ωB97XD, EOM-CCSD, and DLPNO-STEOM-CCSD results were obtained using cc-pVDZ basis set on the PBE0/cc-pVDZ optimized geometry; the SA(6)-CASSCF(4,4), CASPT2(4,4), and XMS-CASPT2(4,4) results were obtained using ANO-S-VDZP basis set on the SA(6)-CASSCF(4,4)/ANO-S-VDZP optimized geometry; the SA(5)-CASSCF(8,7), CASPT2(8,7), and XMS-CASPT2(8,7) results were obtained using ANO-S-VDZP basis set on the SA(5)-CASSCF(8,7)/ANO-S-VDZP optimized geometry.

Table 1 shows that CAM-B3LYP, ωB97XD, EOM-CCSD, and DLPNO-STEOM-CCSD predict consistent vertical excitation energies, excited-state transitions, and oscillator strengths. The predicted vertical excitation energies range from 6.36–6.90, 6.48–7.02, and 6.99–7.42 eV for the S_1, S_2, and S_3 states, respectively. The methods used here agree that the S_1 and S_3 have primarily $\pi\pi^*$ configuration, while S_2 corresponds to a $\sigma\pi^*$ configuration. We compare each method to DLPNO-STEOM-CCSD/cc-pVDZ; the DLPNO-STEOM-CCSD/cc-pVDZ vertical excitation energies to the S_1, S_2, and S_3 state are 6.69, 6.77, and 7.19 eV. The corresponding excitation energies are approximately the average across the different methods (S_1, S_2, and S_3 are 6.61, 6.71, and 7.19 eV, respectively). The predicted oscillator strength is 0.04–0.08 in $S_0 \rightarrow S_1$ and 0.00 in $S_0 \rightarrow S_2$ and $S_0 \rightarrow S_3$. The oscillator strength is 0.08 in $S_0 \rightarrow S_1$, slightly larger than 0.04 obtained from the other methods. Figure 3 shows the molecular orbitals that correspond to the vertical excitations.

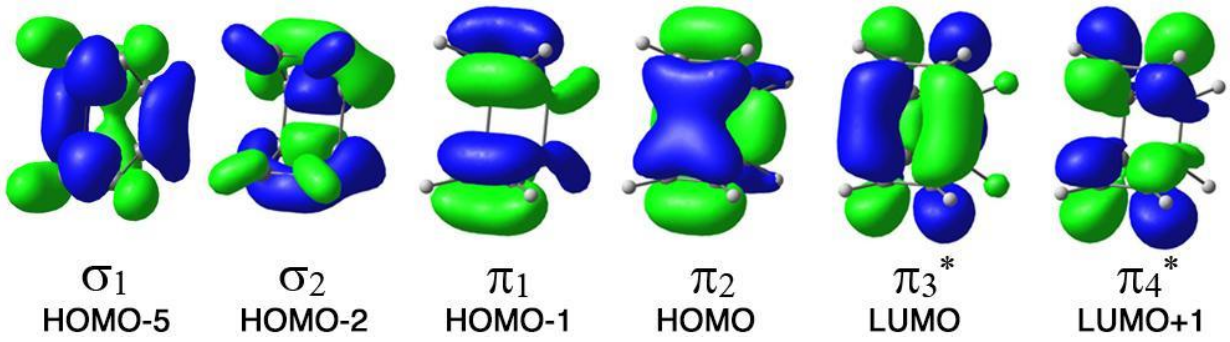

Figure 3. Molecular orbitals of **1-S1-FC** computed with DLPNO-STEOM-CCSD/cc-pVDZ//PBE0/cc-pVDZ. Isosurface value = 0.04.

The $S_0 \rightarrow S_1$ is dominated by a singly-excited highest occupied molecular orbital to lowest unoccupied molecular orbital (HOMO→LUMO or $\pi_2 \rightarrow \pi_{3^*}$) $\pi\pi^*$ configuration, $S_0 \rightarrow S_2$ corresponds to a singly-excited $\sigma\pi^*$ configuration (HOMO-2→LUMO or $\sigma_2 \rightarrow \pi_{3^*}$), and $S_0 \rightarrow S_3$ is contributed by another $\pi\pi^*$ configuration (HOMO→LUMO+1 or $\pi_2 \rightarrow \pi_{4^*}$). We assigned the HOMO and LUMO as π-orbitals (π_2 and π_{3^*}), but they do possess σ-characters of the bridged σ_{CC}-bonds. This suggests that multireference calculations are required to fully describe the photophysics of **1** and will be addressed in the subsequent discussion.

We hypothesized that the chemically intuitive (4,4) active space of **1-S$_0$** would have enough flexibility to account for σ_{CC}-bond formation along with the reaction coordinate.[32] The SA(6)-CASSCF(4,4)/ANO-S-VDZP vertical excitation energies to S_1, S_2, and S_3 are overestimated relative to DLPNO-STEOM-CCSD by 1.74, 1.80, and 1.58 eV, respectively (Table 1). The (4,4) active space incorrectly predicts that the S_1 state is primarily a singly excited $\pi\pi^*$ configuration ($\pi_1 \rightarrow \pi_{3^*}$), in contrast with the $\pi_2 \rightarrow \pi_{3^*}$ transition predicted by DLPNO-STEOM-CCSD. Because the (4,4) active space omits σ-orbitals, the $\pi\pi^*$ configuration is doubly excited in S_2 (π_1, $\pi_2 \rightarrow \pi_{3^*}$, π_{4^*}) instead of a $\sigma\pi^*$-configuration. The $\pi_2 \rightarrow \pi_{3^*}$ transition was found in S_3 with an oscillator strength of 0.48. We were able to partially overcome the limitations of the (4,4) active space by applying perturbative corrections ((XMS-)CASPT2(4,4)/ANO-S-VDZP//CASSCF(4,4)/ANO-S-VDZP). These methods agree that the S_1 and S_3 are dominated by $\pi\pi^*$ configurations, which correspond to $\pi_2 \rightarrow \pi_{3^*}$ and $\pi_2 \rightarrow \pi_{4^*}$ transitions, respectively. The predicted XMS-CASPT2(4,4) vertical excitation energies are 6.51 and 7.22 eV, which almost reproduces the DLPNO-STEOM-CCSD/cc-pVDZ results. However, the $\sigma\pi^*$ configuration in S_2 is still elusive since there are no σ-orbitals in the CASSCF(4,4) reference wavefunction.

We included σ-orbitals and removed the highest-lying and least occupied π-orbital,[33] thus expanding our active space to (8,7). The SA(5)-CASSCF(8,7)/ANO-S-VDZP consistently predicts a singly excited $\pi\pi^*$ configuration ($\pi_2 \rightarrow \pi_{3^*}$) in S_1, thus matching the DLPNO-STEOM-CCSD results. The S_2 and S_3 are dominated by $\pi\pi^*$ and $\sigma\pi^*$ configurations, respectively, with zero oscillator strength. The CASPT2 calculation shows the same $\pi\pi^*$ nature in S_1 as that at the CASSCF level, but the inconsistencies come from the reversed order of S_2 and S_3, relative to the DLPNO-STEOM-CCSD. The CASPT2(8,7)/ANO-S-VDZP//SA(5)-CASSCF(8,7)/ANO-S-VDZP predicts vertical excitation energies for $S_0 \rightarrow S_1$, S_2 and S_3 states to be 6.25, 6.39, and 6.79 eV, respectively. The energetic proximity of S_1 and S_2 (CASPT2 = 0.14 eV) leads to strong coupling between the $\sigma\pi^*$ and $\pi\pi^*$ states. XMS-CASPT2(8,7)/ANO-S-VDZP//SA(5)-CASSCF(8,7)/ANO-S-VDZP predicts a singly excited $\sigma\pi^*$ configuration in S_1 and a singly excited $\pi\pi^*$ configuration in S_2, which disagrees with the DLPNO-STEOM-CCSD. The S_1-S_2 energy difference is larger than the DLPNO-STEOM-CCSD (0.53 vs 0.08 eV, respectively).

We will use CASPT2(8,7)/ANO-S-VDZP energies in subsequent discussions because the single-state CASPT2 correction is closer to the DLPNO-STEOM-CCSD results than the XMS-CASPT2 results. Our benchmarking of single and multi-reference methods has led us to conclude that the dominant excitation pathway of **1** is to and along with the S_1 via HOMO→LUMO transition ($\pi_2 \rightarrow \pi_{3^*}$ in (8,7) active space). We used the CASSCF(8,7)/ANO-S-VDZP model chemistry to study the photophysics and subsequent photochemistry from the S_1 Franck-Condon point, **1-S$_1$-FC**. We, therefore, performed minimum energy path (MEP) calculations to explore the steepest descent path from **1-S$_1$-FC**. The energy profile is shown in Figure 4a.

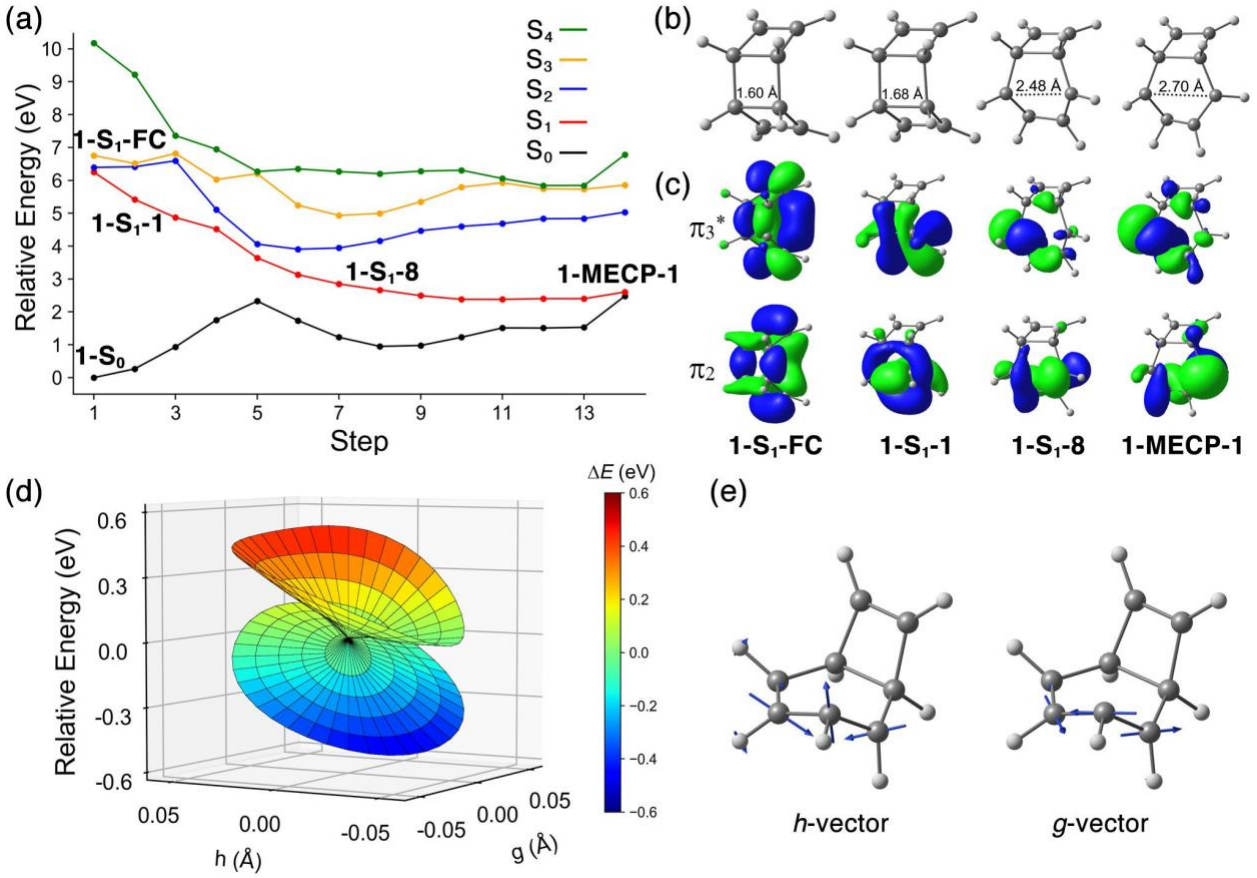

Figure 4. (a) The minimum energy path from **1-S₁-FC** to the S₁/S₀-MECP, **1-MECP-1** at CASPT2(8,7)/ANO-S-VDZP//SA(5)-CASSCF(8,7)/ANO-S-VDZP level of theory. The geometry of **1-MECP-1** was optimized with SA(4)-CASSCF(8,7)/ANO-S-VDZP. (b) The geometries of **1-S₁-FC**, MEP step 2 (**1-S₁-1)**, MEP step 8 (**1-S₁-8**), and **1-MECP-1**. (c) The major contributing molecular orbital to the electronic configuration in S_1: π_2 and π_{3^*} in **1-S₁-FC**, and corresponding orbitals in **1-S₁-1**, **1-S₁-8**, and **1-MECP-1**. Isosurface value = 0.04. (d) The branching plane of the **1-MECP-1** spanned over *g*- and *h*-vector space. (e) The *g*- and *h*-vectors of **1-MECP-1**, the blue arrows represent the positive direction.

The MEP of **1-S₁-FC** ends near the S_1/S_0 degeneracy; we optimized this point to an MECP, **1-MECP-1** that lies 2.48 eV above **1-S₀**. The π_{CC}-bonds of **1** do not approach one another to form cubane, consistent with the experiment. Instead, we observed significant geometrical changes along with the MEP that one bridged σ_{CC}-bond of **1-S₁-FC** elongates from 1.60 Å to 2.70 Å (Figure 4b). This bonding change corresponds to a 4π-disrotatory electrocyclic ring-opening of the fused cyclobutene ring in **1**. The π-orbitals (π_2 and π_{3^*} in Figure 4c) contribute strongly to the overall $\pi\pi^*$ configuration of **1-S₁-FC**; however, the σ-orbitals of the bridged bonds mix with the $\pi\pi^*$ configuration. The mixed σ-orbitals are strongly correlated as bonding and antibonding orbitals in a $\sigma\sigma^*$ excitation, which promotes the σ_{CC}-bond breaking, as illustrated in Figure 4c. In **1-S₁-FC**, the π-orbitals do not satisfy the symmetry requirement and cannot favorably yield [2+2]

cycloadducts. As the σ_{CC}-bond is lengthened to 1.68 Å in **1-S_1-1,** the π-orbitals localize onto the cyclobutene moiety. The correlated σ-orbitals have more nonbonding character in **1-S_2-8** which reduces the S_0–S_1 energy difference towards the **1-MECP-1** crossing point. We characterized the PESs near **1-MECP-1** and found a sloped topology and a single relaxation path in the ground-state surface toward the negative direction of *g*- and *h*-vectors (Figure 4d).

The *g*-vector describes bond stretching between the carbon atoms in the cyclohexadiene ring and the *h*-vector represents an out-of-plane movement of a single carbon atom. The superposition of *g*- and *h*-vectors in their negative direction promote the ring-opening of the fused cyclobutene ring to a cyclohexadiene ring. These static calculations suggest that **1** will undergo ring-opening reaction via **1-MECP-1** to the major product **3**. We sought to understand why the [2+2] photocycloaddition of **1** is not experimentally observed. The potential energy surface was generated via constrained S_1-optimizations along with the *r* and θ parameters and is shown in Figure 5a.

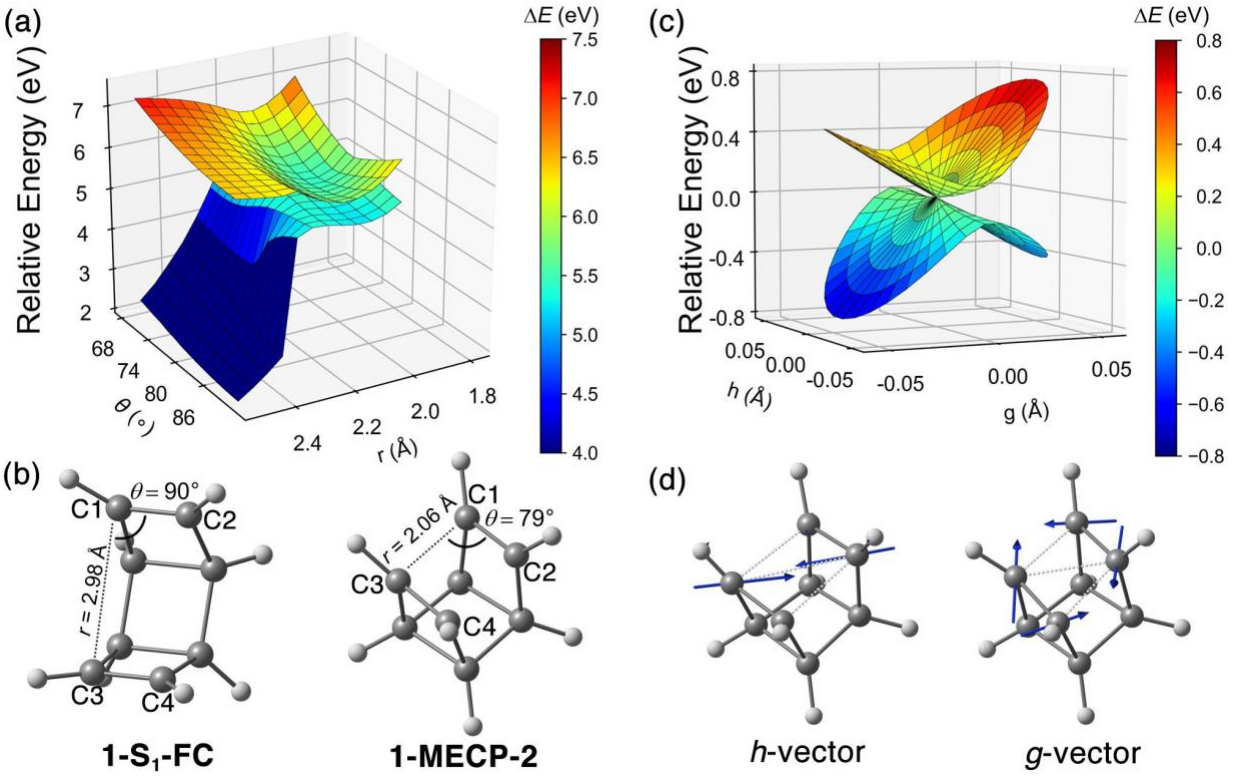

Figure 5. (a) The 2D potential energy surface of **1** in S_1 with the vertical S_0 surface at SA(5)-CASSCF(8,7)/ANO-S-VDZP level of theory. The angle θ is defined by ∠C3-C1-C2 and ∠C3-C4-C2; the distance *r* is defined by r(C1-C2) and r(C3-C4) (b) The SA(5)-CASSCF(8,7)/ ANO-S-VDZP optimized geometries of **1-S_1-FC** and **1-MECP-2** (4.29 eV at CASPT2(8,7)/ ANO-S-VDZP) (c) The branching plane of the **1-MECP-2** spanned over *g*- and *h*-vector space. (d) The *g*- and *h*-vectors of **1-MECP-2**, the blue arrows represent the positive direction.

The reactant **1-S$_0$** is at the point r = 2.98 Å and θ = 90° colored with dark blue corresponding to a local minimum of the 2D PES. We varied the r parameter from 1.56 to 2.98 Å to describe the potential ring-closing reaction to cubane. As r starts at 2.98 Å, the constrained S_1 optimizations converge to a bond-breaking geometry as we have observed in the MEP of **1-S$_1$-FC** because of the similar $\pi\pi^*$ configuration. The CASSCF calculations become unstable due to the negligible multiconfigurational character as r approaches 1.56 Å. We thus shifted our focus to the region of the 2D PES bound by r = 1.9–2.5 Å and θ = 64–85° (Figure 5a). We found a minimum region in the S_1 surface is also an S_1/S_0 degeneracy area bound by r = 2.05–2.15 Å and θ = 76–79° using constrained MECP optimization. We located a second MECP, **1-MECP-2** without geometrical constraints, which lies 4.29 eV above **1-S$_0$**. The optimized geometry of **1-MECP-2** features partially broken C1–C3 and C2–C4 π_{CC}-bond lengths (1.44 Å). The intramolecular distance r is also significantly decreased from 2.98 Å in **1-S$_1$-FC** to 2.06 Å in **1-MECP-2**. The angles θ are 79° (∠C3-C1-C2 and ∠C3-C4-C2) and 101° (∠C1-C2-C4 and ∠C1-C3-C4), which lead to a rhomboidal structure with respect to C1–C4. Figure 5c depicts a PES scan near **1-MECP-2**; the intersection topology shows a characteristic funnel from the excited-state surface to the ground-state. The ground-state relaxation paths are bifurcated to the positive and negative direction of the *g*-vector. Figure 5d shows that the *g*-vector represents the nuclear motions towards bond formation in **2** and the *h*-vector corresponds to the nuclear movement of diagonal carbon atoms. The ground-state MEP calculations from **1-MECP-2** have confirmed the two relaxation paths to **1-S$_0$** and **2** with respect to the *g*-vector.

We used the reaction coordinate diagram to describe the PES near the **1-S$_1$-FC** in the [2+2] cycloaddition pathway via **1-MECP-2**. The reaction coordinate diagram was interpolated according to the optimized geometry of **1-S$_1$-FC**, **1-MECP-2**, and **2**. Figure 6a shows the S_0, S_1, S_2, S_3, and S_4 energies with respect to the aforementioned interpolation scheme.

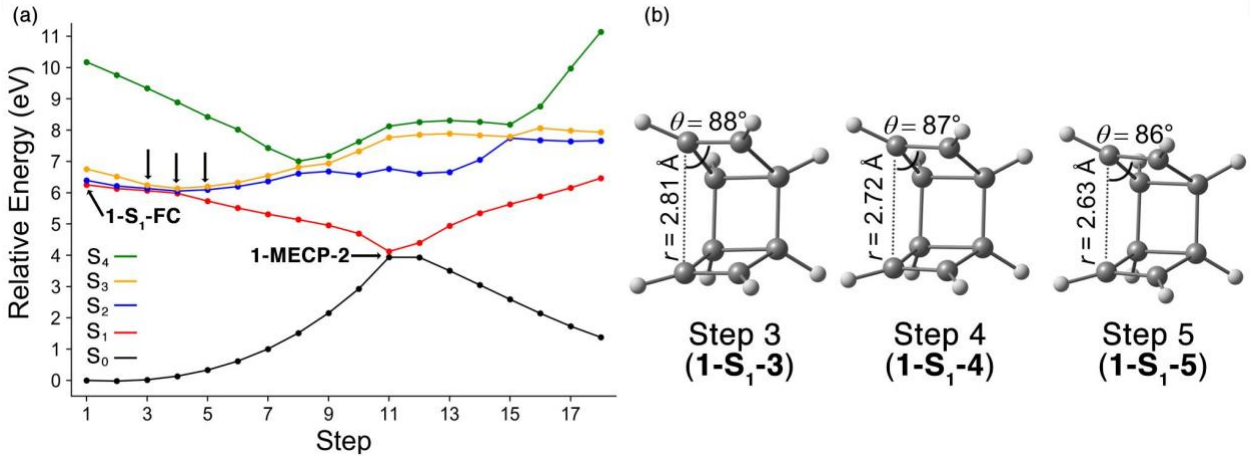

Figure 6. (a) The reaction coordinate diagram from **1-S$_1$-FC** to **2** via **1-MECP-2** at CASPT2(8,7)/ANO-S-VDZP. The geometries of **1-S$_1$-FC** and **1-MECP-2** were optimized at SA(5)-CASSCF(8,7)/ANO-S-VDZP level of theory. The geometry of **2** was optimized with PBE0/cc-pVDZ level of theory because of its negligible multiconfigurational character. Three

points near a crossing region at Step 3–5 are highlighted by black arrows. (b) The geometries of **1-S$_1$-3**, **1-S$_1$-4**, and **1-S$_1$-5** at the interpolation Step 3–5. Further discussions regarding the nature of $\pi\pi^*$ state in Step 3–5 can be found in the supporting information.

The interpolated geometries near **1-S$_1$-FC** (Step 1-5) are nearly degenerate across the first three excited states (S$_1$–S$_3$). The S$_1$, S$_2$, and S$_3$ at Step 4 are 6.30, 6.36, and 6.37 eV, respectively. The energies of S$_2$ and S$_3$ remain nearly degenerate (6.32 and 6.41 eV) but the S$_1$ state is considerably lower (6.07 eV) at Step 5. The interpolated geometries at Step 3–5 are shown in Figure 6b. The *r* parameter is 2.98 Å in **1-S$_1$-FC** and decreased by 0.09 Å per step. As we will discuss in the dynamics section, the geometries corresponding to steps 1–5 are accessible with Wigner-sampling at 300 K.

Our static calculations are unable to enumerate all possible reaction pathways or predict quantum yields. We expanded upon our static mechanistic calculations by performing non-adiabatic molecular dynamics simulations. We generated 1,722 Wigner-sampled non-equilibrium geometries at 300 K and started a 700 fs FSSH-NAMD trajectory on each sampled geometry with SA(5)-CASSCF(8,7)/ANO-S-VDZP. The sampled geometries have *r* and θ parameters that range from 2.71 to 3.27 Å and 78 to 103°, respectively. 85 % (1,471) of the 1,722 trajectories successfully relaxed to the ground-state. Our following discussion on the product statistics and trajectory characterization will not include those trajectories still lying in the excited states. The distributions of observed products and reaction paths are collected in Figure 8.

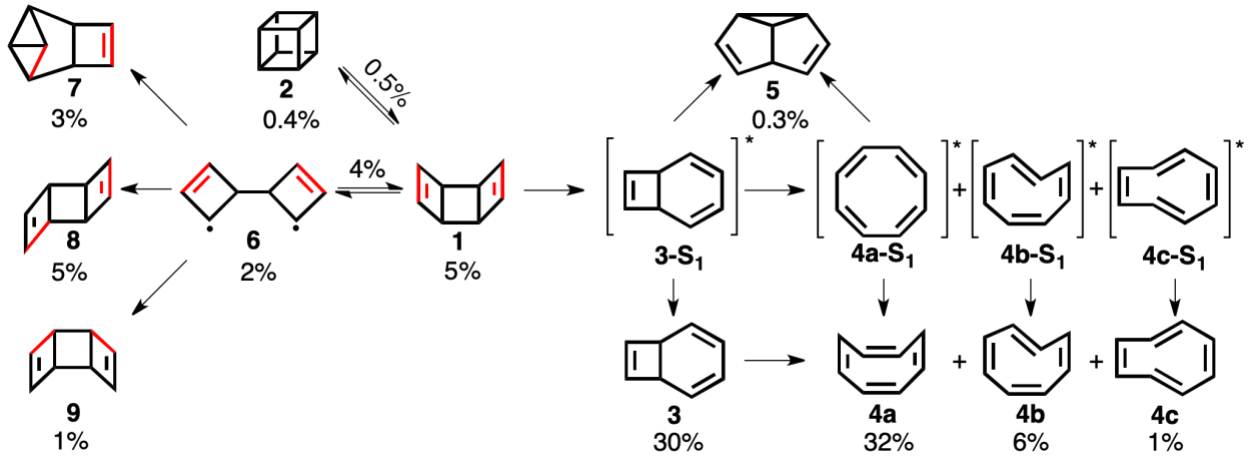

Figure 8. The distributions of 8 observed products and reaction paths in the ~700 fs FSSH-AIMD simulation of **1** at SA(5)-CASSCF(8,7)/ANO-S-VDZP level of theory. **3-S$_1$**, **4a-S$_1$**, **4b-S$_1$**, and **4c-S$_1$** represent possible S$_1$ local minima. **4a, 4b,** and **4c** are isomers of cycloocta-1,3,5,7-tetraenes; **5**: semibullvalene; **6**: bicyclobutenyl diradical. The π_{CC}-bonds in **1** are colored in red to highlight the isomerization from **1** to **6**, **7** (tetracycloocta-7-ene), **8** (*anti*-tricyclo[4,2,0,0$_{2,5}$]octa-3,7-dienes), and **9** (**1** and **9** are the same molecule but have different carbon atoms in the π_{CC}-bonds). The yield was computed as the number of trajectories leading to each structure divided by 1,722 (the total number of trajectories).

Our trajectories show a strong preference for ring-opening (69%) but also identify other possible products (16%). The predicted major products are cycloocta-1,3,5,7-tetraene (COT), **4a** (32%) and **3** (30%). The ring-opening provides a single path to **3-S$_1$**, which is also an intermediate along the isomerization pathways towards the other possible local minima **4a-S$_1$**, **4b-S$_1$**, and **4c-S$_1$** leading to the COT isomers **4a**, **4b**, **4c**, respectively. Approximately 1% trajectories involve a ground-state thermal isomerization from **3** to **4a**. We observe that 0.3% of the trajectories form **5** via **3-S$_1$** or **4a-S$_1$**. The [2+2] cycloaddition path from **1** toward **2** occurred in 0.4% of the trajectories. 0.5% of trajectories passed through the same S$_1$/S$_0$ intersection seam but returned to **1**. This nearly 1:1 ratio agrees with the notable bifurcated relaxation paths from **1-MECP-2**. The ratio between the number of ring-opening trajectories to that of the [2+2] cycloaddition ones is 77:1 (69% *vs.* 0.9%), which substantially supports the highly preferred ring-opening mechanism in our static study. We observed diradical **6** in 16% of the trajectories. These trajectories are bifurcated; 11 % move forward to **6** but 4 % revert to **1** after they cross with the ground-state. Because the two cyclobutene radicals are connected through a single bond in **6**, the diradical can continue to form a new bond. Thus, only 2% trajectories stay in the diradical form throughout the ~700 fs simulation. As the rotation of the single bond (Figure 8), **6** can isomerize to **7** (3%), **8** (5%), and **9** (1%).

We plotted the traces of trajectories in Figure 9 to characterize the geometries in these trajectories and fully explore the photodynamics from **1-S$_1$-FC**.

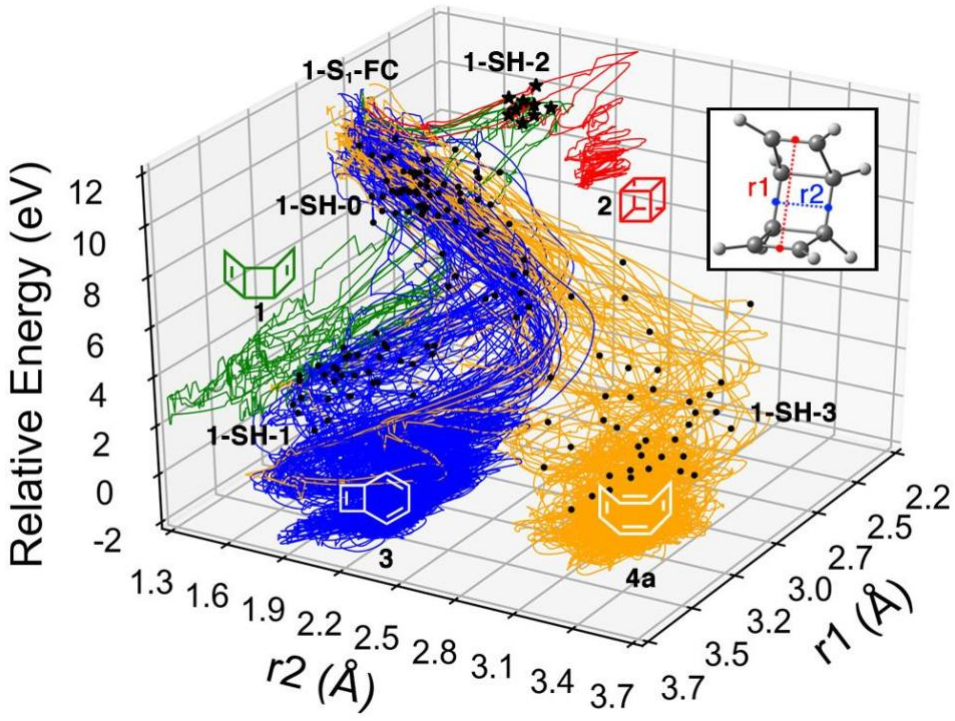

Figure 9. (a) The trajectories of ~700 fs FSSH-AIMD simulation of **1** at SA(5)-CASSCF(8,7)/ANO-S-VDZP level of theory. The r1 is defined by the distance between the centroid of π_{CC}-bonds and the r2 is defined by the distance between the centroid of σ_{CC}-bonds.

We highlight 9 trajectories that correspond to a [2+2] cycloaddition of **1**, where 6 (green) of them return to **1** and 3 (red) move toward **2**. We show 141 trajectories to demonstrate the ring-opening of **1**, where 83 (blue) lead to **3** and 58 (orange) form **4a**. The trajectories also have some surface hopping to the higher excited-state as the energy difference is small at the Franck-Condon region. We used the latest S_1/S_0 surface hopping points to characterize the trajectories, which is more relevant to describe the reaction path to the ground-state products. The latest S_1/S_0 surface hopping points **1-SH-2** in the [2+2] cycloaddition pathways were denoted with black stars; **1-SH-0**, **1-SH-1**, and **1-SH-3** in the ring-opening pathways are marked by dots. The most characteristic geometries of the latest S_1/S_0 surface hopping points are shown in Figure 10.

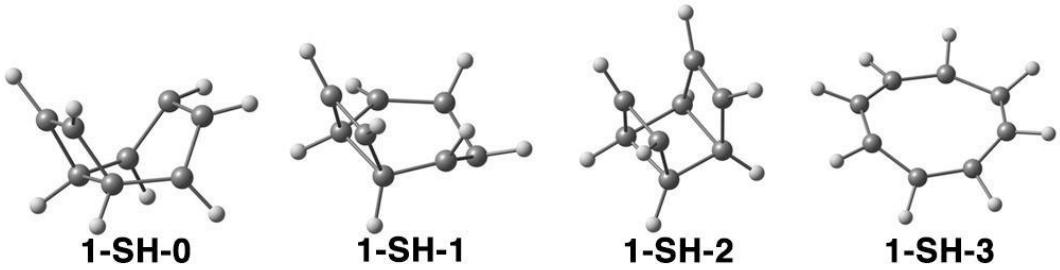

Figure 10. The most characteristic geometries of **1-SH-0**, **1-SH-1**, **1-SH-2**, and **1-SH-3** in ~700 fs FSSH-AIMD simulation of **1** at SA(5)-CASSCF(8,7)/ANO-S-VDZP level of theory.

The geometry of **1-SH-0** is a 'tub' and resembles the geometry of **1-S$_1$-FC**. This suggests that **1-SH-0** represents a higher energy S_1/S_0 crossing seam near **1-S$_1$-FC**. **1-SH-1** has a geometry close to **1-MECP-1** representing the S_1/S_0 crossing seam near the MECP of **1** toward **3**. The geometry of **1-SH-2** is more similar to **1-MECP-2** exhibiting the S_1/S_0 crossing seam close to the MECP of **1** toward **2**. **1-SH-3** shows a cyclooctatetraene ring geometry corresponding to the formation of **4a**.

We describe the ring-opening process with the reaction coordinates r1 and r2. Figure 9 shows two stages in the ring-opening trajectories toward **3** and **4a**. In the first stage, the r2 increases from ~1.60 to ~2.50 Å and ~3.40 Å for **3** and **4a**, respectively but the r1 has smaller changes about 0.30 Å (from ~2.80 to ~3.10 Å). The steeper rate of change of r2 agrees with the preferential bridged σ_{CC}-bond-breaking identified with the MEP from **1-S$_1$-FC**. In the second stage, the r2 ranges from 2.20–2.50 Å and 3.00–3.40 Å for **3** and **4a**, respectively. The r1, however, increases from ~2.80–3.10 to ~3.50 and 3.20 Å for **3** and **4a**, respectively. The structures continue to relax beyond the initial ring-opening step. The **3** → **4a** thermal isomerization was identified by overlaying the ground state trajectories in Figure 9.

Our FSSH-NAMD trajectories have revealed that [2+2] cycloaddition pathways from **1-S$_1$-FC** are possible via **1-SH-2**. Figure 11a and 11b show the snapshots of geometries at critical time points that confirm the findings of the static reaction coordinate diagram interpolation. The reaction coordinate r1 decreases from ~2.77–3.00 Å at **1-S$_1$-FC** to ~2.00–2.20 Å at the latest S_1/S_0 surface

hopping points **1-SH-2**. Then the trajectories bifurcate to **2** forming two new σCC-bonds (r1 = ~1.60 Å) or to **1** (the r1 elongates to ~3.00 Å).

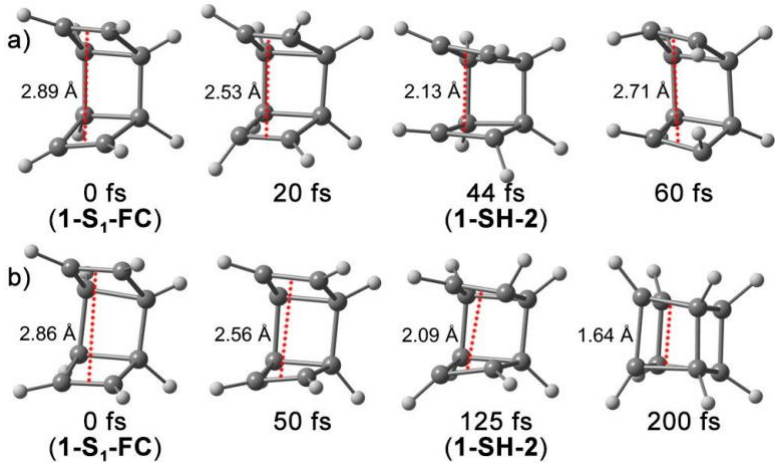

Figure 11. Snapshots of geometries in the [2+2] cycloaddition trajectories in ~700 fs FSSH-AIMD simulation of **1** at SA(5)-CASSCF(8,7)/ANO-S-VDZP level of theory. The trajectories revert to **1** in (a) and move forward to **2** in (b). The r1 parameters are shown in red dotted lines.

Overall, the breaking of the bridge *σ*CC-bond(s) releases significant strain energy causing the ring-opening trajectories to significantly diverge from the trajectories leading to cubane. The trajectories leading to cubane are less sloped because increasing strain energy competes with electronic stabilization from the FC-region. The cycloaddition trajectories are closely spaced because they follow a singular path from **1-S1-FC** to **1-SH-2**. Our FSSH-NAMD trajectories suggest that while the 4π-disrotatory electrocyclic ring-opening mechanism of **1** is preferred, the cycloaddition is theoretically possible but in exceedingly small yields.

Concluding Remarks

Our multiconfigurational static and dynamic multiconfigurational computations offer a comprehensive analysis of the photophysics and photochemistry of **1**. The vertical excitation energy of **1** is 6.25 eV and is a HOMO→LUMO ππ* excitation ($\pi_2 \rightarrow \pi_{3^*}$) with CASPT2(8,7)/ANO-S-VDZP//CASSCF(8,7)/ANO-S-VDZP. These results were benchmarked against CAM-B3LYP/cc-pVDZ, ωB97XD/cc-pVDZ, EOM-CCSD/cc-pVDZ, DLPNO-STEOM-CCSD/cc-pVDZ. The πCC- and σCC-orbitals mix in the S_1 (ππ*) state promotes the σCC-bond breaking. Our 2D PES scan helped to locate a region of degeneracy and a rhomboidal MECP that connects **1** and **2**, suggesting that a cycloaddition is theoretically possible. However, MEP calculations pointed towards a 4π-disrotatory electrocyclic ring-opening of **1** rather than [2+2] cycloaddition. Our interpolated reaction path confirmed that the [2+2] cycloaddition of **1** is not forbidden but requires **1** to be in a non-equilibrium geometry featuring a shorter intramolecular π-π distance (2.72 Å), which changes the nature of ππ* state to satisfy the orbital symmetry. The

MEP of **1** from the S_1 Franck-Condon point has identified a more favorable path marked by a steeper descent to the ring-opening pathway.

Acknowledging the limited information that can be gleaned from a potential energy surface scan or MEP, we performed unprecedented dynamics simulations to determine other possible reaction pathways. The initial conditions were sampled with the Wigner method at 300 K and 1,722 ~700 fs trajectories were started from S_1-FC points. These simulations yielded a wealth of information about the predicted major and minor products. 85% (1,471) of the trajectories relaxed to 8 products that show the ring-opening is the dominant pathway (69%). The major products are **3** (30%) and **4a** (32%). Only 0.4% of trajectories undergo [2+2] cycloaddition to form cubane. This agrees with our static photochemical mechanism study. Current efforts in the group are focused on substituent effects on **1** to rational design the derivatives of **1** that preferentially form cubanes.

Acknowledgment

We acknowledge Dr. Jordan M. Cox, Daniel Adrion, Prof. Noah Z. Burns, and Prof. Todd J. Martinez for helpful discussion. We acknowledge the Office of Naval Research (ONR N00014-12-1-0828) for funding this research. We appreciate the assistance from the Northeastern Research Computing Team and access to the computing resources of the Discovery cluster.

References

1. M. D. Karkas, J. A. Porco, Jr. and C. R. Stephenson, *Chem. Rev.*, **2016**, *116*, 9683-9747.
2. D. Cambie, C. Bottecchia, N. J. Straathof, V. Hessel and T. Noel, *Chem. Rev.*, **2016**, *116*, 10276-10341.
3. K. Hull, J. Morstein and D. Trauner, *Chem. Rev.*, **2018**, *118*, 10710-10747.
4. (a) J. Calbo, C. E. Weston, A. J. White, H. S. Rzepa, J. Contreras-Garcia and M. J. Fuchter, *J. Am. Chem. Soc.*, **2017**, *139*, 1261-1274; (b) A. K. Saydjari, P. Weis and S. Wu, *Adv. Energy Mater.*, **2017**, *7*.
5. (a) M. V. Roux, J. Z. Davalos, P. Jimenez, R. Notario, O. Castano, J. S. Chickos, W. Hanshaw, H. Zhao, N. Rath, J. F. Liebman, B. S. Farivar and A. Bashir-Hashemi, *J. Org. Chem.*, **2005**, *70*, 5461-5470; (b) M. V. Roux, G. Martín-Valcarcel, R. Notario, S. Kini, J. S. Chickos and J. F. Liebman, *J. Chem. Eng. Data*, **2011**, *56*, 1220-1228.
6. P. E. Eaton, *Angew. Chem. Int. Ed.*, **1992**, *31*, 1421-1436.
7. in *CRC Handbook of Chemistry and Physics*, ed. W. M. Haynes, CRC Press LLC, Boca Raton: FL, 94 edn., 2013-2014, pp. 3-438.
8. (a) Z. Li and S. L. Anderson, *The Journal of Physical Chemistry A*, **2003**, *107*, 1162-1174; (b) H.-D. Martin, T. Urbanek, P. Pföhler and R. Walsh, *J. Chem. Soc., Chem. Commun.*, **1985**, , 964-965.
9. H. T. Huang, L. Zhu, M. D. Ward, B. L. Chaloux, R. Hrubiak, A. Epshteyn, J. V. Badding and T. A. Strobel, *J Phys Chem Lett*, **2018**, *9*, 2031-2037.
10. R. Okude, G. Mori, A. Yagi and K. Itami, *Chem. Sci.*, **2020**, DOI: 10.1039/d0sc01909g.
11. P. E. Eaton and T. W. Cole, *J. Am. Chem. Soc.*, **1964**, *86*, 962-964.

12. R. Gleiter and S. Brand, *Chem. Eur. J.*, **1998**, *4*, 2532-2538.
13. R. Gleiter and M. Karcher, *Angew. Chem. Int. Ed.*, **1988**, *27*, 840-841.
14. L. F. Pelosi and W. T. Miller, *J. Am. Chem. Soc.*, **1976**, *98*, 4311-4312.
15. A. de Meijere, S. Redlich, D. Frank, J. Magull, A. Hofmeister, H. Menzel, B. Konig and J. Svoboda, *Angew. Chem. Int. Ed. Engl.*, **2007**, *46*, 4574-4576.
16. R. Gleiter, K.-H. Pfeifer and W. Koch, *J. Comput. Chem.*, **1995**, *16*, 31-36.
17. M. J. S. Dewar, E. G. Zoebisch, E. F. Healy and J. J. P. Stewart, *J. Am. Chem. Soc.*, **1985**, *107*, 3902-3909.
18. (a) S. Brand and R. Gleiter, *Tetrahedron Lett.*, **1997**, *38*, 2939-2942; (b) R. Gleiter and S. Brand, *Tetrahedron Lett.*, **1994**, *35*, 4969-4972.
19. I. Fdez Galvan, M. Vacher, A. Alavi, C. Angeli, F. Aquilante, J. Autschbach, J. J. Bao, S. I. Bokarev, N. A. Bogdanov, R. K. Carlson, L. F. Chibotaru, J. Creutzberg, N. Dattani, M. G. Delcey, S. S. Dong, A. Dreuw, L. Freitag, L. M. Frutos, L. Gagliardi, F. Gendron, A. Giussani, L. Gonzalez, G. Grell, M. Guo, C. E. Hoyer, M. Johansson, S. Keller, S. Knecht, G. Kovacevic, E. Kallman, G. Li Manni, M. Lundberg, Y. Ma, S. Mai, J. P. Malhado, P. A. Malmqvist, P. Marquetand, S. A. Mewes, J. Norell, M. Olivucci, M. Oppel, Q. M. Phung, K. Pierloot, F. Plasser, M. Reiher, A. M. Sand, I. Schapiro, P. Sharma, C. J. Stein, L. K. Sorensen, D. G. Truhlar, M. Ugandi, L. Ungur, A. Valentini, S. Vancoillie, V. Veryazov, O. Weser, T. A. Wesolowski, P. O. Widmark, S. Wouters, A. Zech, J. P. Zobel and R. Lindh, *J. Chem. Theory Comput.*, **2019**, *15*, 5925-5964.
20. (a) K. Pierloot, B. Dumez, P.-O. Widmark and B. r. O. Roos, *Theor. Chim. Acta*, **1995**, *90*, 87-114; (b) R. Pou-Amérigo, M. Merchán, I. Nebot-Gil, P.-O. Widmark and B. O. Roos, *Theor. Chim. Acta*, **1995**, *92*, 149-181; (c) P.-O. Widmark, P.-k. Malmqvist and B. r. O. Roos, *Theor. Chim. Acta*, **1990**, *77*, 291-306; (d) P.-O. Widmark, B. J. Persson and B. r. O. Roos, *Theor. Chim. Acta*, **1991**, *79*, 419-432.
21. (a) B. O. Roos and K. Andersson, *Chem. Phys. Lett.*, **1995**, *245*, 215-223; (b) B. O. Roos, K. Andersson, M. P. Fülscher, L. Serrano-Andrés, K. Pierloot, M. Merchán and V. Molina, *J. MOL. STRUC-THEOCHEM*, **1996**, *388*, 257-276.
22. T. Yanai, D. P. Tew and N. C. Handy, *Chem. Phys. Lett.*, **2004**, *393*, 51-57.
23. J. D. Chai and M. Head-Gordon, *J. Chem. Phys.*, **2008**, *128*, 084106.
24. J. F. Stanton and R. J. Bartlett, *J. Chem. Phys.*, **1993**, *98*, 7029-7039.
25. R. Berraud-Pache, F. Neese, G. Bistoni and R. Izsak, *J. Chem. Theory Comput.*, **2020**, *16*, 564-575.
26. T. H. Dunning, *J. Chem. Phys.*, **1989**, *90*, 1007-1023.
27. (a) J. P. Perdew, K. Burke and M. Ernzerhof, *Phys. Rev. Lett.*, **1996**, *77*, 3865-3868; (b) J. P. Perdew, K. Burke and M. Ernzerhof, *Phys. Rev. Lett.*, **1997**, *78*, 1396-1396.
28. F. Neese, *Wiley Interdisciplinary Reviews: Computational Molecular Science*, **2012**, *2*, 73-78.
29. M. J. Frisch, G. W. Trucks, H. B. Schlegel, G. E. Scuseria, M. A. Robb, J. R. Cheeseman, G. Scalmani, V. Barone, G. A. Petersson, H. Nakatsuji, X. Li, M. Caricato, A. V. Marenich, J. Bloino, B. G. Janesko, R. Gomperts, B. Mennucci, H. P. Hratchian, J. V. Ortiz, A. F. Izmaylov, J. L. Sonnenberg, Williams, F. Ding, F. Lipparini, F. Egidi, J. Goings, B. Peng, A. Petrone, T. Henderson, D. Ranasinghe, V. G. Zakrzewski, J. Gao, N. Rega, G. Zheng, W. Liang, M. Hada, M. Ehara, K. Toyota, R. Fukuda, J. Hasegawa, M. Ishida, T. Nakajima, Y. Honda, O. Kitao, H. Nakai, T. Vreven, K. Throssell, J. A. Montgomery Jr., J. E. Peralta, F. Ogliaro, M. J. Bearpark, J. J. Heyd, E. N. Brothers, K. N. Kudin, V. N. Staroverov, T.

A. Keith, R. Kobayashi, J. Normand, K. Raghavachari, A. P. Rendell, J. C. Burant, S. S. Iyengar, J. Tomasi, M. Cossi, J. M. Millam, M. Klene, C. Adamo, R. Cammi, J. W. Ochterski, R. L. Martin, K. Morokuma, O. Farkas, J. B. Foresman and D. J. Fox, *Journal*, 2016.

30. G. J. Martyna, M. E. Tuckerman, D. J. Tobias and M. L. Klein, *Mol. Phys.*, **1996**, *87*, 1117-1157.
31. Z. Zara, J. Iqbal, K. Ayub, M. Irfan, A. Mahmood, R. A. Khera and B. Eliasson, *J. Mol. Struct.*, **2017**, *1149*, 282-298.
32. F. Bernardi, A. Bottoni, M. A. Robb, H. B. Schlegel and G. Tonachini, *J. Am. Chem. Soc.*, **1985**, *107*, 2260-2264.
33. (a) J. Kim, H. Tao, T. J. Martinez and P. Bucksbaum, *J. Phys. B: At., Mol. Opt. Phys.*, **2015**, *48*, 164003; (b) J. Kim, H. Tao, J. L. White, V. S. Petrovic, T. J. Martinez and P. H. Bucksbaum, *J. Phys. Chem. A*, **2012**, *116*, 2758-2763; (c) H. Tao, First Principles Molecular Dynamics and Control of Photochemical Reactions. Ph.D. thesis; Stanford University, **2011**.